CrossMark

J̶M PAPERS

Cohesive sediment: intermediate shear produces maximum aggregate size

K. Zhao[1,2], B. Vowinckel[2,3], T.-J. Hsu[4], B. Bai[1],† and E. Meiburg[2],†

[1]State Key Laboratory of Multiphase Flow in Power Engineering, Xi'an Jiaotong University, Xi'an 710049, PR China

[2]Department of Mechanical Engineering, UC Santa Barbara, CA 93106, USA

[3]Leichtweiß-Institut für Wasserbau, Technische Universität Braunschweig, 38106 Braunschweig, Germany

[4]Center for Applied Coastal Research, Department of Civil and Environmental Engineering, University of Delaware, Newark, DE 19716, USA

We interpret the Taylor–Green cellular vortex model in terms of the Kolmogorov length and velocity scales, in order to study the balance between aggregation and breakup of cohesive sediment in fine-scale turbulence. One-way coupled numerical simulations, which capture the effects of cohesive, lubrication and direct contact forces on the flocculation process, reproduce the non-monotonic relationship between the equilibrium floc size and shear rate observed in previous experiments. The one-way coupled results are confirmed by select two-way coupled simulations. Intermediate shear gives rise to the largest flocs, as it promotes preferential concentration of the primary particles without generating sufficiently strong turbulent stresses to break up the emerging aggregates. We find that the optimal intermediate shear rate increases for stronger cohesion and smaller particle-to-fluid density ratios, and we propose a simple model for the equilibrium floc size that agrees well with experimental data reported in the literature.

Key words: suspensions, sediment transport, cohesive sediments

1. Introduction

The aggregation of cohesive particles in turbulence depends on such quantities as particle size, density and volume fraction, as well as on the cohesive force strength and the turbulent shear rate. Experimental studies have provided substantial insight into key aspects of the flocculation process, although the role of the shear rate remains somewhat controversial. The pioneering work by Winterwerp ([1998]) found that the equilibrium floc size $D_{f,eq}$ scales inversely with the turbulent shear rate G, *viz.* $D_{f,eq} \sim G^{-0.5}$.

† Email addresses for correspondence: bfbai@xjtu.edu.cn, meiburg@engineering.ucsb.edu

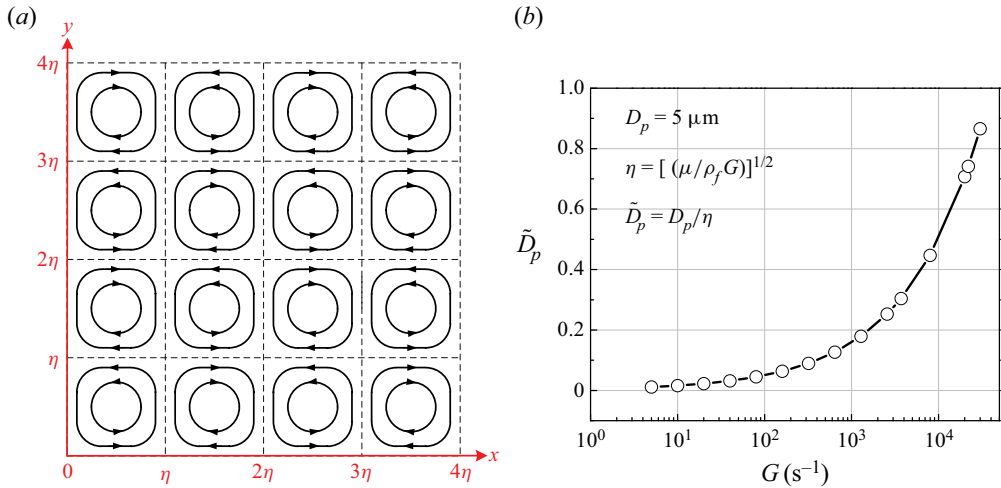*K. Zhao, B. Vowinckel, T.-J. Hsu, B. Bai and E. Meiburg*

Figure 1. (*a*) Streamlines of the spatially periodic, two-dimensional cellular Taylor–Green vortex flow. (*b*) The relationship between the dimensionless particle size $\tilde{D}_p$ and the shear rate G in the present simulations.

Most subsequent experiments confirmed that $D_{f,eq}$ decreases for larger G (Spicer *et al.* 1998; Soos *et al.* 2008; Bubakova, Pivokonsky & Filip 2013; Zhang *et al.* 2019). On the other hand, several authors observed the opposite trend of larger flocs for stronger shear in flows with low shear (He *et al.* 2012; Wang *et al.* 2018). Dyer (1989) introduced the concept of a maximum floc size at intermediate shear, while emphasizing the need for further investigation. Serra, Colomer & Logan (2008) speculated that for low-shear flows the preferential concentration of sediment by turbulence dominates over the breakage of aggregates, so that stronger shear promotes larger flocs. Mietta *et al.* (2009) discussed the role of experimental error, and they argued that it is difficult to keep particles suspended in low-shear flow due to settling, so that the flocculation process may be incomplete in experimental devices with limited depth.

The current investigation aims to shed light on the above issues by employing particle-resolving numerical simulations that can capture the interplay of hydrodynamic, inertial and inter-particle forces during the growth, deformation and breakup of flocs. In the spirit of earlier investigations by Maxey (1987), Bergougnoux *et al.* (2014) and Zhao *et al.* (2020), we will employ one-way coupled simulations of two-dimensional, steady, spatially periodic Taylor–Green vortices (with fluid density ρ_f and dynamic viscosity μ), cf. figure 1(*a*). For a few select parameter combinations we will compare the one-way coupled results with two-way coupled simulations. The shear rate and Reynolds number associated with this flow are $G = U/\eta$ and $Re = \eta U \rho_f/\mu$, where η and U are the characteristic length and velocity scales of the cellular vortex flow, respectively. In order to investigate behaviour at viscous scales of turbulence, we fix $Re = 1$ which yields $\eta = \sqrt{\mu/(\rho_f G)}$ and $U = \sqrt{\mu G/\rho_f}$.

2. Physical and computational model

We analyse the one-way coupled motion of small cohesive spherical particles in cellular flow fields given by the streamfunction

$$\psi = \frac{U\eta}{\pi^2} \sin\left(\frac{\pi x}{\eta}\right) \sin\left(\frac{\pi y}{\eta}\right), \tag{2.1}$$

and the corresponding fluid velocity $\boldsymbol{u}_f = (u_f, v_f)^{\mathrm{T}}$. We employ this fluid velocity field as a conceptually simple model of the fine-scale structure of turbulence, so that we associate η and U with the Kolmogorov length and velocity scales. We consider a flow with N spherical particles of identical diameter D_p and density ρ_p, with particle i having translational velocity $\boldsymbol{u}_{p,i} = (u_{p,i}, v_{p,i})^{\mathrm{T}}$ and angular velocity $\omega_{p,i}$. We focus on particles with $D_p > 2\,\mu\mathrm{m}$, so that we can neglect Brownian motion (Chen, Li & Marshall 2019). The physical and computational approach for tracking the particle motion is described in detail in Zhao *et al.* (2020), so that we only provide a brief summary here.

By choosing η, U and ρ_f as the characteristic length, velocity and density scales, the dimensionless fluid velocity field can be expressed as

$$\tilde{u}_f = \frac{1}{\pi} \sin(\pi\tilde{x})\cos(\pi\tilde{y}), \quad \tilde{v}_f = -\frac{1}{\pi}\cos(\pi\tilde{x})\sin(\pi\tilde{y}), \tag{2.2a,b}$$

while the dimensionless equations for the motion of the primary particles take the form

$$\tilde{m}_p\frac{\mathrm{d}\tilde{\boldsymbol{u}}_{p,i}}{\mathrm{d}\tilde{t}} = \underbrace{-\frac{\tilde{m}_p(\tilde{\boldsymbol{u}}_{p,i} - \tilde{\boldsymbol{u}}_{f,i})}{St}}_{\tilde{F}_{d,i}} + \sum_{j=1,j\neq i}^{N}(\tilde{\boldsymbol{F}}_{con,ij} + \tilde{\boldsymbol{F}}_{lub,ij} + \tilde{\boldsymbol{F}}_{coh,ij}), \tag{2.3}$$

$$\tilde{I}_p\frac{\mathrm{d}\tilde{\omega}_{p,i}}{\mathrm{d}\tilde{t}} = \sum_{j=1,j\neq i}^{N}(\tilde{\boldsymbol{T}}_{con,ij} + \tilde{\boldsymbol{T}}_{lub,ij}), \tag{2.4}$$

where dimensionless quantities are denoted by tildes. The dimensionless mass of a particle is defined as $\tilde{m}_p = \pi\tilde{D}_p^3\rho_s/6$, its moment of inertia as $\tilde{I}_p = \pi\rho_s\tilde{D}_p^5/60$ and the solid-to-fluid density ratio according to $\rho_s = \rho_p/\rho_f$. $\tilde{\boldsymbol{F}}_{con,ij}$, $\tilde{\boldsymbol{F}}_{lub,ij}$ and $\tilde{\boldsymbol{F}}_{coh,ij}$ denote the direct contact, lubrication and cohesive forces, with details given in Biegert, Vowinckel & Meiburg (2017), Zhao *et al.* (2020) and Vowinckel *et al.* (2019), respectively. Johnson & Greenwood (1997) suggested that the present additive adhesion/collision modelling framework is valid for collisions with a Tabor parameter value $\mu_T < 0.1$. As analysed in Appendix A, the Tabor parameter is quite small in the present simulations, $\mu_T < 0.03$, which indicates that the present modelling framework is appropriate. This is also consistent with the findings of Yao & Capecelatro (2021), who demonstrated that the additive adhesion/collision modelling framework is valid when the Tabor parameter $\mu_T \leq 0.98$.

We introduce a pseudo-volume fraction of the particles as $\phi = (\pi\tilde{D}_p^3 N)/(6\tilde{L}_x\tilde{L}_y\tilde{D}_p)$, where $\tilde{L}_x$ and $\tilde{L}_y$ represent the dimensionless width and height of the computational domain. The Stokes number is defined as

$$St = \frac{Re\rho_s\tilde{D}_p^2}{18} = \frac{\rho_s\tilde{D}_p^2}{18}, \tag{2.5}$$

and indicates the ratio of inertial to viscous forces acting on a particle. We remark that the Reynolds number $Re = \eta U\rho_f/\mu$ formed with the length and velocity scales of an individual cellular vortex equals unity, so that these cellular vortices are indeed representative of the Kolmogorov scales of a turbulent flow field. Consequently, we obtain for the dimensionless particle diameter $\tilde{D}_p = D_p\sqrt{\rho_f G/\mu}$. Hence, for constant dimensional particle size D_p, viscosity μ and density ρ_f, we explore the influence of the dimensional shear G by varying $\tilde{D}_p$.

The cohesive force is normalized by the inertial force of a fluid element at the Kolmogorov scale. The strength of the dimensionless cohesive force is captured by the cohesive number

$$Co = \max(\|\tilde{\boldsymbol{F}}_{coh,ij}\|) = \frac{\max(\|\boldsymbol{F}_{coh,ij}\|)}{U^2\eta^2\rho_f} = \frac{A_H D_p \rho_f}{16\lambda\zeta_0\mu^2}, \qquad (2.6)$$

where the range of the cohesive force $\lambda = D_p/20$ and the microscopic size of surface asperities $\zeta_0 = 0.00025D_p$, consistent with Zhao *et al.* (2020). The Hamaker constant A_H is a function of the particle and fluid properties, representative values of A_H for common natural systems can be found in Vowinckel *et al.* (2019). We remark that the dimensional values D_p, μ and ρ_f are fixed in the present simulations, so that the cohesive number Co is determined by A_H.

To summarize, the independent dimensionless simulation inputs are the particle diameter $\tilde{D}_p$, the volume fraction ϕ of the particles, the density ratio ρ_s and the cohesive number Co. Note that the Stokes number St does not constitute an independent parameter, as it is determined by $\tilde{D}_p$ and ρ_s. Hence, our choice of the Kolmogorov scales as the characteristic scales of the flow field reduces the number of independent parameters by one, compared with the earlier work of Zhao *et al.* (2020). The range over which the physical and dimensionless parameters varied in the simulations is provided in table 1. Shear rates vary in the range $6\,\text{s}^{-1} \leq G \leq 3700\,\text{s}^{-1}$, which covers both natural sediment transport conditions ($5\,\text{s}^{-1} \leq G \leq 600\,\text{s}^{-1}$, Tran, Kuprenas & Strom 2018), as well as many industrial processes including coating, spraying, lubrication and injection moulding ($G < 5000\,\text{s}^{-1}$, Christopher, Trushant & Gareth 2008). The ratio of the Kolmogorov length scale to primary particle size, η/D_p, takes values up to $O(80)$, which covers common sediment transport applications (Markussen & Andersen 2014; Strom & Keyvani 2016). The range of particle volume fractions corresponds to typical sediment transport applications (Serra *et al.* 2008). The range of the turbulent dissipation rate $\epsilon = \mu^3/(\rho_f^3\eta^4)$ is presented as well. As mentioned above, for a constant dimensional particle size D_p, fluid viscosity μ and density ρ_f, we have $\tilde{D}_p \sim \sqrt{G}$, cf. figure 1(*b*), so that we can investigate the influence of varying the dimensional shear rate G by modifying $\tilde{D}_p$. The range of the Hamaker constant A_H in our simulations, $10^{-21}\,\text{J} < A_H < 10^{-18}\,\text{J}$, covers common natural sediment applications, and even cloud processes (Chen *et al.* 2019; Vowinckel *et al.* 2019).

3. Flocculation dynamics of aggregates

We analyse ensembles of $N = 100$ particles in order to obtain insight into their flocculation dynamics. Table 2 summarizes the combinations of domain size $\tilde{L}_x \times \tilde{L}_y$, pseudo-volume fraction ϕ and dimensionless particle diameter $\tilde{D}_p$ considered. For each of these combinations we simulated the four density ratios $\rho_s = 2.65$, 5, 8 and 10, along with the six Co values of 0.002, 0.005, 0.013, 0.05, 0.2 and 0.5, resulting in a total of 360 simulations. In each simulation, all of the particles have identical diameters and densities, and they are initially at rest and separate from each other. The domain size increases for cases with larger particles, yielding similar volume fractions (except cases L9 and L10).

In order to accelerate the evolution of the equilibrium stage, we initially place the particles randomly within a small rectangular subsection of the overall computational domain. The wide and the length of the subsection are defined as L_{ix} and L_{iy}, respectively. For cases L1–11 with relatively small particles, this subsection consists of a thin strip in the y-direction, as shown by the slightly transparent spheres in figure 2(*a*). For cases L12–15

Physical parameters

Particle diameter	D_p	$5\,\mu$m
Particle density	ρ_p	2650–10 000 kg m^{-3}
Dynamic viscosity	μ	1.0×10^{-3} Pa s
Fluid density	ρ_f	1000 kg m^{-3}
Shear rate	G	6–3700 s^{-1}
Kolmogorov length scale	η	16.44–408.25 μm
Kolmogorov velocity scale	U	2.45×10^{-3}–6.08×10^{-2} m s^{-1}
Turbulent dissipation rate	ϵ	3.60×10^{-5}–13.69 m^2 s^{-3}
Hamaker constant	A_H	2.0×10^{-21}–5.0×10^{-19} J

Dimensionless parameters

Density ratio	ρ_s	2.65–10
Particle diameter	$\tilde{D}_p$	1.22×10^{-2}–3.04×10^{-1}
Volume fraction of particles	ϕ	3.60×10^{-5}–3.27×10^{-4}
Cohesive number	Co	2.0×10^{-3}–5.0×10^{-1}
Stokes number	St	2.21×10^{-5}–5.13×10^{-2}

Table 1. Range of physical parameters employed in the present work. The independent dimensionless inputs are ρ_s, $\tilde{D}_p$, ϕ and Co.

Case	$\tilde{L}_x \times \tilde{L}_y$	ϕ	$\tilde{D}_p$
L1	14×14	4.01×10^{-5}	1.22×10^{-2}
L2	20×20	3.60×10^{-5}	1.66×10^{-2}
L3	24×24	3.64×10^{-5}	2.00×10^{-2}
L4	26×26	3.87×10^{-5}	2.24×10^{-2}
L5	32×32	3.83×10^{-5}	2.74×10^{-2}
L6	38×38	3.63×10^{-5}	3.16×10^{-2}
L7	42×42	3.71×10^{-5}	3.54×10^{-2}
L8	60×60	3.64×10^{-5}	5.00×10^{-2}
L9	40×40	8.18×10^{-5}	5.00×10^{-2}
L10	20×20	3.27×10^{-4}	5.00×10^{-2}
L11	100×100	3.93×10^{-5}	8.66×10^{-2}
L12	144×144	3.79×10^{-5}	1.22×10^{-1}
L13	200×200	3.93×10^{-5}	1.73×10^{-1}
L14	280×280	4.01×10^{-5}	2.45×10^{-1}
L15	360×360	3.74×10^{-5}	3.04×10^{-1}

Table 2. Dimensionless parameters of the flocculation simulations.

with larger particles, the area into which we initially place the particles is shaped like a square. We will demonstrate below that the influence of the initial particle configuration on the equilibrium number of flocs is negligible. Figure 2(*a*) shows a few typical floc configurations for case L7, with $Co = 0.5$, $\rho_s = 2.65$ and $\tilde{D}_p = 3.54 \times 10^{-2}$, at time $\tilde{t} = 95$, distinguished by colour. We recognize that some flocs have a compact structure (black, green and red), while others are more loosely aggregated (blue).

3.1. *Flocculation and equilibrium stages*

Consistent with our earlier work (Zhao *et al.* 2020, 2021), we consider different particles to belong to the same floc if their surface distance is less than half the range of the
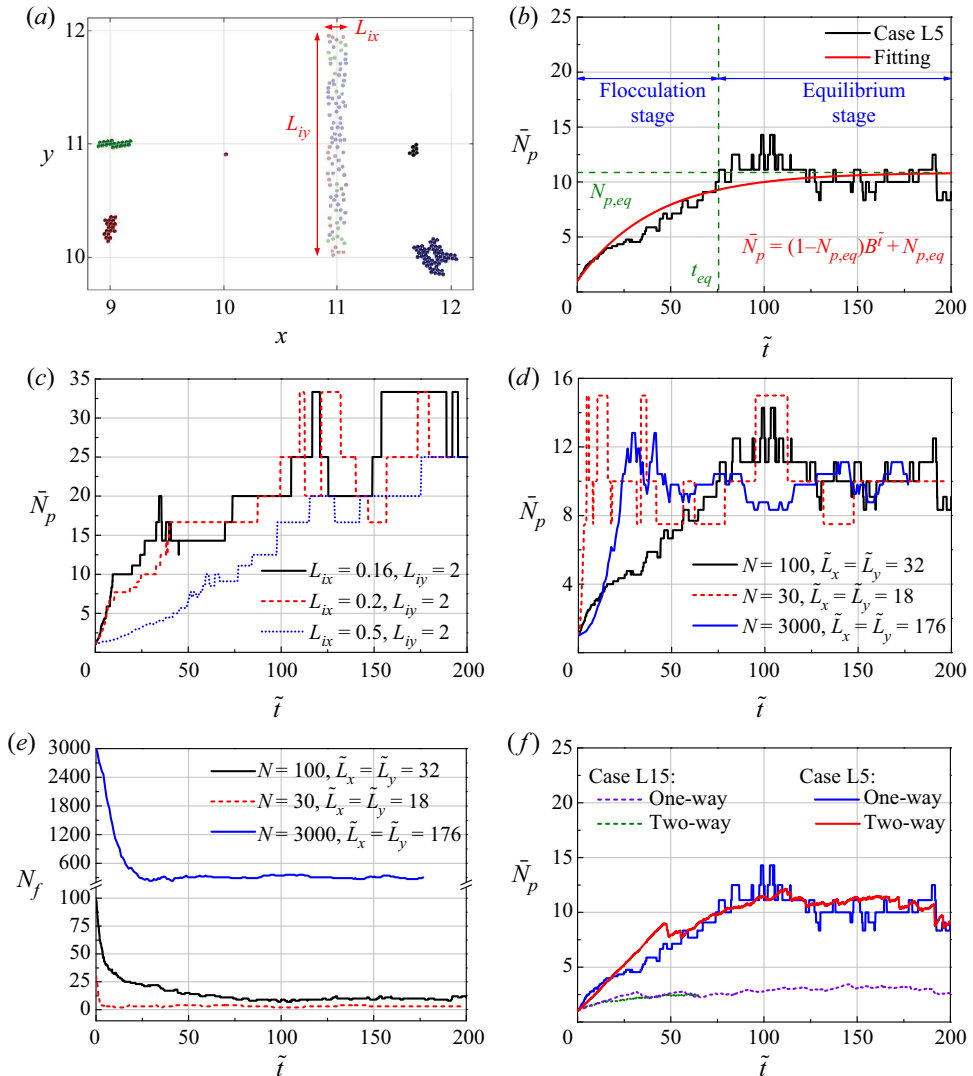
Figure 2. (*a*) Typical floc configurations observed at $\tilde{t} = 95$ for case L7 with $Co = 0.5$, $\rho_s = 2.65$ and $\tilde{D}_p = 3.54 \times 10^{-2}$. Initially, the primary particles, shown as slightly transparent spheres, are randomly placed within a subsection of width $L_{ix} = 0.16$ and length $L_{iy} = 2$. (*b*) Temporal evolution of the average number of primary particles per floc $\bar{N}_p$ for the typical case L5 with $Co = 0.5$ and $\rho_s = 2.65$. Simulation data and a least-squares fit according to (3.1) are shown, with $N_{p,eq}$ and t_{eq} denoting the equilibrium value of $\bar{N}_p$ and the beginning of the equilibrium stage, respectively. (*c*) Influence of the initial particle distribution on the flocculation for the typical case L7, with $Co = 0.5$ and $\rho_s = 2.65$. The initial particle distribution affects only the duration of the transient flocculation stage, but not the average floc size during the equilibrium stage. (*d*) Influence of the number of primary particles on the equilibrium floc size for the typical case L5, with $\rho_s = 2.65$, $Co = 0.5$ and $\phi \approx 3.8 \times 10^{-5}$. The equilibrium floc size is found to be largely independent of the number of primary particles. (*e*) Influence of the number of primary particles on the number of flocs for the typical case L5. (*f*) Temporal evolution of the average number of primary particles per floc $\bar{N}_p$ for typical cases L15 and L5 with $\rho_s = 2.65$, $Co = 0.5$ and $\phi \approx 4 \times 10^{-5}$. Comparisons between one-way coupled simulations and equivalent, fully two-way coupled simulations show good agreement.

cohesive force. In terms of a physical force balance, breakage occurs when the net force pulling the particles apart is sufficiently strong to overcome the maximum of the cohesive force holding the particles together. Figure 2(*b*) shows the temporal evolution of the average number of primary particles per floc $\bar{N}_p$ for the representative case L5, with $\rho_s = 2.65$ and $Co = 0.5$. We remark that an individual particle is considered to be the smallest possible floc. As the primary particles aggregate, $\bar{N}_p$ increases rapidly with time from its initial value of one, before levelling off around a constant value $N_{p,eq}$ that reflects a stable equilibrium between aggregation and breakage. Hence, we observe two distinct stages of the flow, *viz.* an initial flocculation stage and a subsequent equilibrium stage, consistent with previous experimental observations (Winterwerp *et al.* 2006; Son & Hsu 2008; Tran *et al.* 2018).

In order to obtain a quantitative criterion for the ending of the flocculation stage and the beginning of the equilibrium stage, we employ a fitting model for $\bar{N}_p$ of the form

$$\bar{N}_p = (1 - N_{p,eq})B^{\tilde{t}} + N_{p,eq}. \tag{3.1}$$

A least-squares fit yields the coefficient $B = 0.9766$ and the equilibrium average floc size $N_{p,eq} = 10.87$ for case L5, with a coefficient of determination value *R*-squared of 0.8. We define the first instant when $\bar{N}_p = N_{p,eq}$ as the beginning of the equilibrium stage t_{eq}, as shown in figure 2(*b*).

3.2. *Influence of the initial particle configuration on the flocculation dynamics*

We carefully assessed the influence of the initial particle distribution on the flocculation dynamics by varying the width L_{ix} in figure 2(*a*). We note that all particles are initially at rest and separate from each other. Figure 2(*c*) shows the evolution of the average number of primary particles per floc $\bar{N}_p$ for case L7, for various initial distributions. The density ratio and the cohesive number are fixed as $\rho_s = 2.65$ and $Co = 0.5$. We find that while a more dilute initial particle distribution slows down the flocculation process, it does not affect the average equilibrium floc size, which is the focus of the present investigation.

3.3. *Influence of the primary particle number*

To assess the influence of the number of primary particles on the equilibrium floc size, we compared simulations with $N = 30$–3000 initial particles. Figure 2(*d*) presents the evolution of the average number of primary particles per floc $\bar{N}_p$ for different *N*. Figure 2(*e*) shows the evolution of the number of flocs N_f for different *N* accordingly. The primary particle size, the density ratio and the cohesive number are kept constant at $\tilde{D}_p = 2.74 \times 10^{-2}$, $\rho_s = 2.65$ and $Co = 0.5$. The domain size $\tilde{L}_x \times \tilde{L}_y$ varies with *N*, to keep the particle volume fraction fixed at $\phi \approx 3.8 \times 10^{-5}$. The initial local particle concentration was different in all three simulations, yielding different transient behaviours. The equilibrium floc size $N_{p,eq}$ reflecting the balance between breakage and aggregation depends only on the number of primary particles per unit domain when other governing parameters are fixed. We find that $N_{p,eq}$ is statistically independent of the number of primary particles *N* once $N > N_{p,eq}$. The fluctuations of the average floc size during the equilibrium stage become smaller with for increasing particle numbers. This confirms that the value $N = 100$ employed in most of our simulations is sufficient for obtaining insight into the equilibrium stage of small flocs such as those considered here.

3.4. *Comparison of flocculation dynamics in one-way and two-way coupled simulations*

The one-way coupled simulation approach outlined above does not account for the effect of the particles on the fluid motion. Several previous investigations had considered the influence of two-way coupling, such as the shielding of the innermost particles in a large floc, which can have a major impact on the agglomerate breakup (Dizaji & Marshall 2017; Chen *et al.* 2019). In order to demonstrate the ability of the one-way coupled approach to capture the aggregation of small flocs, we now provide a comparison between one-way and two-way coupled simulations. For the two-way coupling approach, we employ the immersed boundary method implemented in Vowinckel *et al.* (2019) to describe the particle–fluid interactions, and we use the spectral approach of Eswaran & Pope (1988) to generate statistically stationary turbulence. We remark that the present one-way coupled approach is sometimes referred to as 'three-way coupled', while the current two-way coupling is also regarded as 'particle-resolved four-way coupling' by some previous researchers (Zhu *et al.* 2022). Additional information on the two-way coupled simulations is provided in Appendix B.

Figure 2(*f*) presents the temporal evolution of $\bar{N}_p$ for typical cases L5 and L15, with $\rho_s = 2.65$ and $Co = 0.5$. When the flocculation is relatively weak (such as case L15 shown by dashed lines), the evolution of $\bar{N}_p$ is very similar for the one-way and two-way coupled simulations, since the modification of the local fluid flow by small flocs with few primary particles is limited. When the flocculation becomes stronger (such as case L5 shown by solid lines), two-way coupling results in a somewhat faster floc growth, although the average floc size during the equilibrium stage, $N_{p,eq}$, which is the focus of the present investigation, remains very similar. We conclude that one-way coupled simulations are able to provide insight into the aggregation of small flocs such as those considered here. Consequently, the one-way coupled Taylor–Green flow provides an efficient approach for analysing the formation of moderate-size flocs in turbulence. We expect that two-way coupled simulations will be required for analysing the dynamics of very large flocs (Yao & Capecelatro 2021).

3.5. *Influence of the governing parameters*

Recall that for a constant dimensional particle size and fluid properties, $\tilde{D}_p \sim \sqrt{G}$, so that we can assess the influence of the dimensional shear rate G by varying $\tilde{D}_p$. Towards this end, figure 3(*a*) demonstrates the influence of $\tilde{D}_p$, and hence G, on the average equilibrium floc size $N_{p,eq}$ for $Co = 0.002$ and $Co = 0.5$, respectively. The other parameters are kept constant at $\rho_s = 2.65$ and $\phi \approx 4 \times 10^{-5}$. As $\tilde{D}_p$ (and hence the shear rate G) increases, $N_{p,eq}$ grows at first, then peaks and subsequently decays. Consequently, the simulations demonstrate that, for primary particles of the same size, intermediate shear rates produce the largest average floc size. This represents a central finding of the present investigation, and is consistent with previous experimental observations by He *et al.* (2012), Serra *et al.* (2008) and Wang *et al.* (2018), who analysed the influence of the shear rate on the average floc size for different sediment types. For certain fluid/sediment combinations, these authors reported the existence of an optimal intermediate shear rate that gives rise to the largest average floc size. Figure 3(*a*) furthermore shows that, as Co increases, the peak value of $N_{p,eq}$ grows and shifts to larger shear rates. Figure 3(*b*) presents $N_{p,eq}$ as function of the Stokes number St, for the same Co, ρ_s and ϕ as figure 3(*a*).

Figure 4(*a*) presents the average equilibrium floc size $N_{p,eq}$ as a function of the shear rate, for different density ratios ρ_s, with $Co = 0.002$ and $\phi = 4 \times 10^{-5}$. For larger ρ_s,
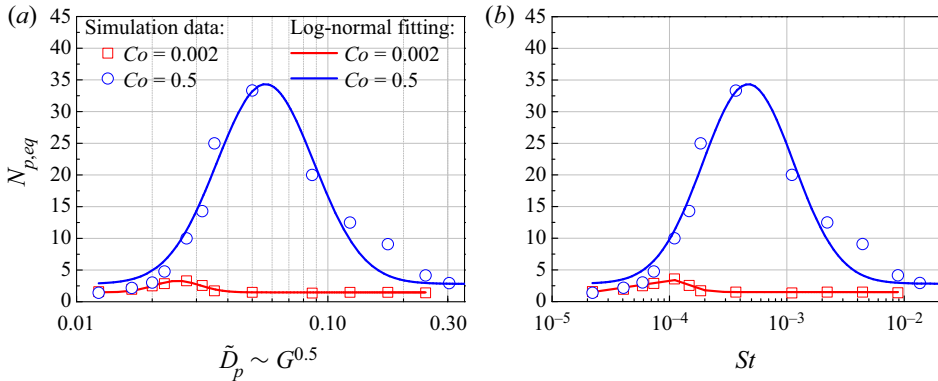
Figure 3. (*a*) Equilibrium value $N_{p,eq}$ as function of the shear rate G, for different Co values, with $\rho_s = 2.65$ and $\phi \approx 4 \times 10^{-5}$; (*b*) $N_{p,eq}$ as function of the Stokes number St, with the same ρ_s and ϕ as (*a*). The relationship closely follows a log-normal distribution.

the peak value of $N_{p,eq}$ grows and shifts to smaller $\tilde{D}_p$ (and hence smaller shear rates). Figure 4(*b–d*) shows a non-monotonic relationship between $N_{p,eq}$ and St, for $\rho_s = 5, 8, 10$, respectively. By comparing cases L8, L9 and L10 for fixed values of ρ_s and Co (not shown), we find that the pseudo-volume fraction ϕ only weakly affects $N_{p,eq}$. This finding agrees with experimental observations by Serra *et al.* (2008), who performed experiments at different particle volume fractions ($2.0 \times 10^{-5} < \phi < 1.0 \times 10^{-4}$), without noticing appreciable differences in $N_{p,eq}$ for the same shear rate.

In order to obtain insight into the mechanisms responsible for the non-monotonic relationship between $\tilde{D}_p$ and $N_{p,eq}$, we keep track of the evolution of three different types of flocs over a suitably specified time interval $\Delta\tilde{t} = 2$: (*a*) those flocs that maintain their identity, i.e. they consist of the same primary particles at the start and the end of the time interval; (*b*) those that add additional primary particles while keeping all of their original ones; and (*c*) all others, i.e. all those that have undergone a breakage event during the time interval. We define the fractions of these respective groups as θ_{id}, θ_{ad} and θ_{br}, with $\theta_{id} + \theta_{ad} + \theta_{br} = 1$. Figure 5 shows the evolution of θ_{br} and θ_{ad} for the three cases L1 ($\tilde{D}_p = 1.22 \times 10^{-2}$), L5 ($\tilde{D}_p = 2.74 \times 10^{-2}$) and L11 ($\tilde{D}_p = 8.66 \times 10^{-2}$), respectively, with fixed values $Co = 0.002$, $\rho_s = 2.65$ and $\phi \approx 4 \times 10^{-5}$. It clearly demonstrates that floc collisions and break-up processes remain active throughout the entire simulations. The red symbols in figure 3(*a*) show that of these three cases L5 has the largest average equilibrium floc size. Figure 5(*a*) shows that θ_{br} generally increases with $\tilde{D}_p$, while, figure 5(*b*) demonstrates that for the early flocculation stage ($\tilde{t} < 10$) the intermediate case L5 has the largest fraction of growing flocs. At this intermediate value of $\tilde{D}_p$, the primary particles rapidly aggregate, but the turbulent stresses are not large enough to easily break the flocs.

3.6. *Limitation of the aggregate size by the vortex size*

In order to capture the physical floc size in the two-dimensional cellular Taylor–Green vortex flow, we define a characteristic scale L_f of the floc as

$$L_f = 2\max(\|\boldsymbol{x}_{p,i} - \boldsymbol{x}_c\|) + D_p, \quad 1 \leqslant i \leqslant N, \tag{3.2}$$
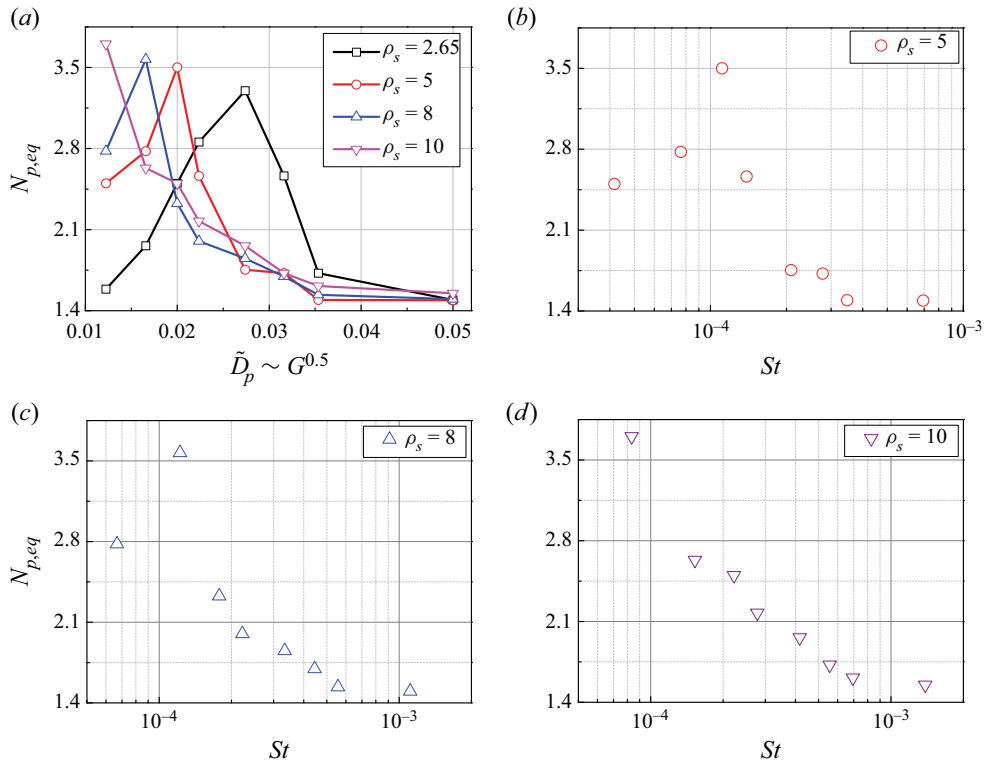
Figure 4. (*a*) Equilibrium value $N_{p,eq}$ as a function of the dimensionless particle size $\tilde{D}_p$ (proportional to $G^{0.5}$), for different density ratios ρ_s. (*b–d*) Show the relation between $N_{p,eq}$ and the Stokes number St for $\rho_s = 5, 8, 10$, respectively. The cohesive number $Co = 0.002$ and the pseudo-volume fraction $\phi \approx 4 \times 10^{-5}$ are fixed.
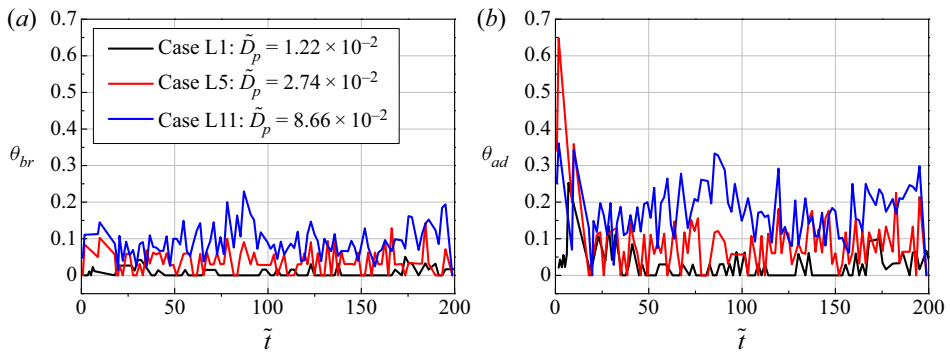

Figure 5. Temporal evolution of the fraction of flocs that over the time interval $\Delta \tilde{t} = 2$, with $Co = 0.002$, $\rho_s = 2.65$, $\phi \approx 4 \times 10^{-5}$, (*a*) undergo breakage; (*b*) add primary particles.

where $x_{p,i}$ denotes the position of the centre of primary particle i, and $x_c = \sum_{i=1}^{N} x_{p,i}/N$ is the floc's centre of mass. We remark that L_f is known as the Feret diameter of flocs in turbulent flow.

We track the average value $\bar{L}_f$ and the maximum value $\max(L_f)$ of floc size with time. Figure 6(*a*) displays the temporal evolution of size ratio between flocs and the individual vortex, with $Co = 0.5$, $\rho_s = 2.65$, $\tilde{D}_p = 5.00 \times 10^{-2}$ and $\phi = 3.64 \times 10^{-5}$. The average
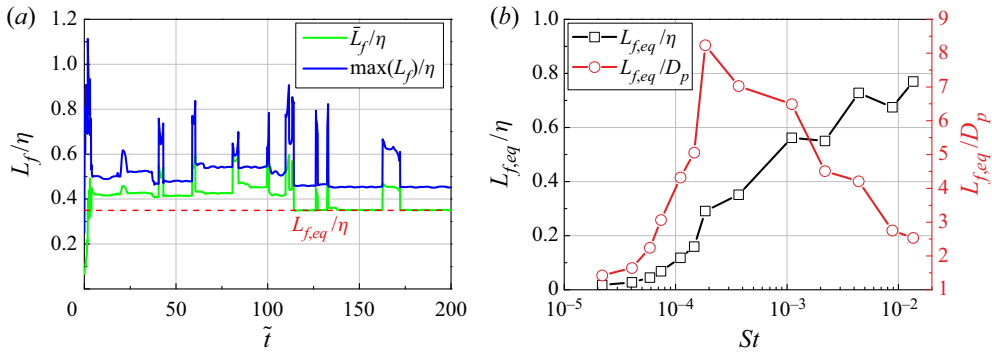
965 A5-10

Figure 6. (*a*) Temporal evolution of the ratio between the physical floc size L_f and the Kolmogorov length scale η, for $Co = 0.5$, $\rho_s = 2.65$, $\tilde{D}_p = 5.00 \times 10^{-2}$, $\phi = 3.64 \times 10^{-5}$. Here, $\bar{L}_f$ and $\max(L_f)$ denote the average floc size and the maximum floc size at time $\tilde{t}$, respectively. (*b*) Ratio between the equilibrium floc size $L_{f,eq}$ and the Kolmogorov length scale η, as well as between $L_{f,eq}$ and the dimensional diameter of primary particles D_p, for different Stokes numbers St, with $Co = 0.5$, $\rho_s = 2.65$, $\phi \approx 4 \times 10^{-5}$.

floc size remains smaller than the Kolmogorov length scale ($\bar{L}_f/\eta < 1$), while the size of the biggest floc can temporarily exceed η before rapidly decreasing. This finding is consistent with previous experimental observations by Stricot *et al.* (2010) and Braithwaite *et al.* (2012), who found that big flocs cannot resist the turbulent stresses for long, and that they are torn apart quickly. For sufficiently strong turbulence the median floc size should be of the same order as the smallest turbulent eddies.

Figure 6(*b*) shows the ratio between the equilibrium floc size $L_{f,eq}$ and the Kolmogorov length scale η for different Stokes numbers St, with $Co = 0.5$, $\rho_s = 2.65$ and $\phi \approx 4 \times 10^{-5}$. Within the present range of parameters shown in table 1, the equilibrium floc size remains smaller than the physical size of an individual vortex. The relation between the length ratio $L_{f,eq}/D_p$ and the Stokes number St is shown as well. As the dimensional size of the primary particles D_p is fixed, we find that intermediate St (and hence intermediate shear rate) produces the maximum physical floc size $L_{f,eq}$, similar to figure 3(*b*) in which the floc size is given in terms of the number of particles.

3.7. *Floc size distribution during the equilibrium stage*

Figure 7 displays the equilibrium floc size distribution for different values of $\tilde{D}_p$, i.e. different shear rates. The other parameters are approximately constant. Here, N_p denotes the number of primary particles in a floc, while $L_{f,eq}/D_p$ represents the physical size ratio between the floc and the primary particle and N_f indicates the number of flocs. Figure 7(*a*,*b*) indicates that the distribution peaks at small size values for the largest and the smallest $\tilde{D}_p$, while it shifts to larger values of floc size for intermediate values of $\tilde{D}_p$. This is consistent with our earlier observation that the average equilibrium floc size has a maximum for intermediate values of $\tilde{D}_p$, cf. figures 3(*a*) and 6(*d*).

3.8. *A model for the average floc size during the equilibrium stage*

According to Khelifa & Hill (2006), for flocs with fractal dimension n_f, the mean equilibrium floc size is related to the average number of primary particles per floc as

$$\tilde{D}_{f,eq} = \tilde{D}_p N_{p,eq}^{1/n_f}. \tag{3.3}$$
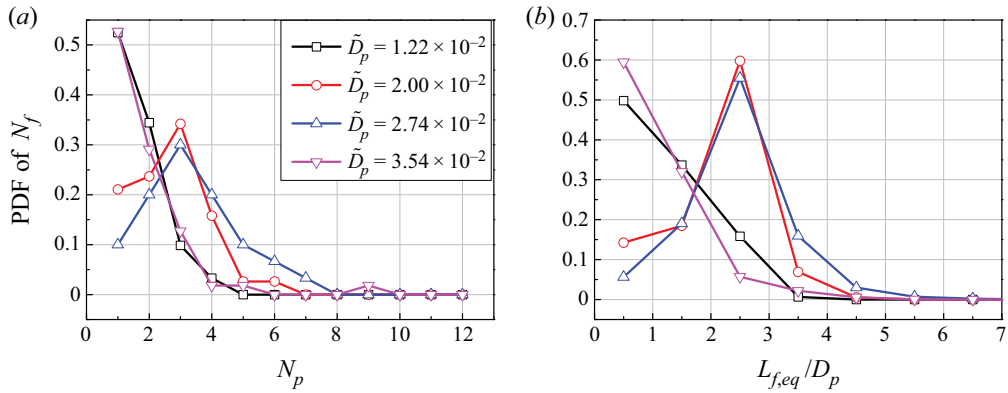
965 A5-11

Figure 7. Equilibrium floc size distribution for different $\tilde{D}_p$. Here, $\rho_s = 2.65$, $\phi \approx 4 \times 10^{-5}$, $Co = 0.002$. (a) Floc size is in terms of the number of primary particles per floc N_p. (b) Floc size is denoted by the size ratio $L_{f,eq}/D_p$.

Figure 3(a) suggests that the relation between $\tilde{D}_p$ and $N_{p,eq}$ can be fitted by a log-normal probability density function of the form

$$N_{p,eq} = ad_2 + \frac{bd_2}{\sigma\sqrt{2\pi}\tilde{D}_p d_1} \exp\frac{-[\ln(\tilde{D}_p d_1) - c]^2}{2\sigma^2},\tag{3.4}$$

where a, b, d_1 and d_2 represent empirical coefficients, while c denotes the mean and σ the standard deviation of the natural logarithm of $\tilde{D}_p$, respectively. The simulation results over the parameter ranges given in table 2 are processed via a least-squares fit, we obtain

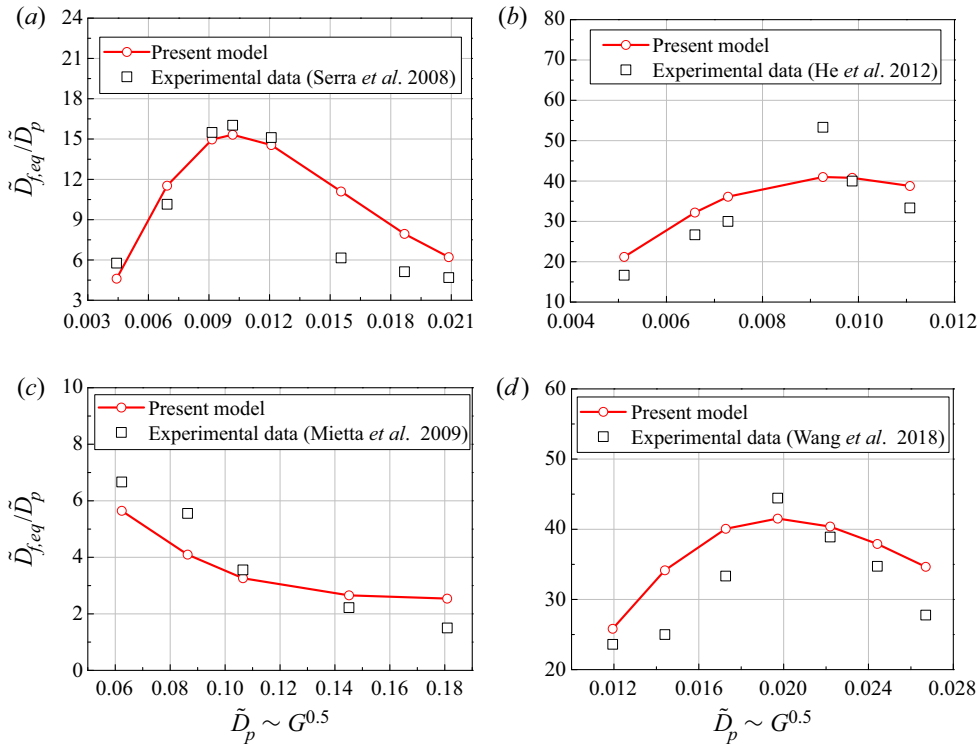$$a^{-1} = 0.0924 + 0.0129(\ln Co)^2 + 3.628\exp(-\rho_s),\tag{3.5}$$

$$b^{-1} = 1.455 - 0.9718\ln Co - 23.66\exp(-\rho_s),\tag{3.6}$$

$$c^{-1} = -0.2727 + 0.2080Co\ln Co,\tag{3.7}$$

$$\sigma^{-1} = 4.729 + 1.504\rho_s^2\ln\rho_s - 1.109\rho_s^{2.5}.\tag{3.8}$$

For the present cellular model flow the values $d_1 = d_2 = 1$ in (3.4) yield optimal agreement with the simulation data, with a fitting deviation of $\pm 30\%$. For real turbulent flows, we can determine d_1 and d_2 by calibrating with available experimental data by other investigators, as follows. In order to capture representative sediment transport applications, we employ the data from four sets of experiments described in the literature, cf. figure 8, which yields the values of d_1 and d_2. We note that our simulations explore the influence of all of the experimental parameters except the pH value, whose influence will be investigated in a future study. As seen in figure 8, $d_2 = 5$ captures all of the experiments, while d_1 varies within the range from 0.5 to 3.5. In summary, the simulation results indicate that the present model (3.3)–(3.8) can successfully predict the average equilibrium floc size for a wide range of sediment transport applications characterized by the dimensionless input parameters $\tilde{D}_p$, ρ_s, Co and d_1. These capture the influence of the particle size, shear strength, density ratio and cohesive force, respectively. Once the model has been calibrated for one particular fluid/particle combination and a given flow field, it is expected to be used to predict the floc size distributions for the same fluid/particle combination at different volume fractions, particle sizes and turbulence properties.

965 A5-12

Figure 8. Calibration of the empirical coefficients d_1 and d_2 in the present model with experimental data. (*a*) Experiments of Serra *et al.* (2008) for latex particles in salt water ($n_f = 2$, $A_H = 1.3 \times 10^{-20}$ J), yield $d_1 = 3$. (*b*) Experiments of He *et al.* (2012) for a Kaolin clay suspension ($n_f = 1.12$, $A_H = 5.0 \times 10^{-20}$ J), yield $d_1 = 3.5$. (*c*) Experiments of Mietta *et al.* (2009) for natural mud in an estuary ($n_f = 2$, $A_H = 1.0 \times 10^{-20}$ J), yield $d_1 = 0.5$. (*d*) Experiments by Wang *et al.* (2018) for a Kaolin clay solution with humic acid ($n_f = 1.12$, $A_H = 5.0 \times 10^{-20}$ J), yield $d_1 = 1.7$. Noted that all of the experiments yield the constant $d_2 = 5$. For details of the experiments, we refer the reader to the cited works.

4. Conclusions

We have presented one-way coupled simulations to study the influence of the shear rate on the flocculation of suspended cohesive particles in a model turbulent flow field. For select parameter combinations, the one-way coupled results were confirmed by two-way coupled simulations. The computational model captures Stokes drag, cohesion, lubrication and direct contact forces. After a transient flocculation stage, we observe a statistically steady equilibrium stage where aggregation and breakage balance each other. The simulations reproduce the non-monotonic relationship between the equilibrium floc size and the turbulent shear rate observed by earlier experiments. They suggest that an intermediate shear rate results in the largest flocs, as it promotes preferential concentration of the primary particles without producing sufficiently large stresses to break up the emerging aggregates. We find that this optimal intermediate shear grows for stronger cohesion and smaller density ratios, while it does not exhibit a strong influence of the particle volume fraction. The relationship between the equilibrium floc size and the shear rate displays a log-normal shape, which enables us to propose a model for predicting the equilibrium floc size for different shear rates. Upon calibration with several experimental data sets, the

proposed model yields good agreements with measured data across a wide range of fluid and sediment properties.

Declaration of interests. The authors report no conflict of interest.

Author ORCIDs.
ⓘ B. Vowinckel https://orcid.org/0000-0001-6853-7750;
ⓘ B. Bai https://orcid.org/0000-0002-6412-4390;
ⓘ E. Meiburg https://orcid.org/0000-0003-3670-8193.

Appendix A. Elastic deformation of cohesive spheres

Two distinct frameworks have been developed for modelling cohesive forces: (i) the Derjaguin–Muller–Toporov (DMT) framework, in which forces are additive because particles do not overlap substantially (Derjaguin, Muller & Toporov 1975); and (ii) the Johnson–Kendall–Roberts (JKR) framework, where the cohesive forces scale with the contact area and particles deform upon contact (Johnson, Kendall & Roberts 1971). The Tabor parameter μ_T helps to decide between those two frameworks, as it reflects the ratio of the elastic deformation and the cohesive interaction range (Tabor 1977)

$$\mu_T = \left(\frac{R_{ij}(\Delta\gamma)^2}{E^{*2}z_0{}^3} \right)^{1/3}. \tag{A1}$$

Here, the reduced particle radius $R_{ij} = D_p/4$, the work of adhesion $\Delta\gamma = 2\gamma$, the combined elastic modulus of the spheres $E^* = E/2(1 - \nu_T{}^2)$, the effective elastic modulus E and the Poisson number ν_T. Chen *et al.* (2019) described the equilibrium separation as $z_0 = (9\pi\gamma R_{ij}{}^2/E)^{1/3}$. Yao & Capecelatro (2021) expressed the surface energy of the particle as $\gamma = A_H/24\pi\delta^2$. Marshall & Li (2014) defined the length $\delta = 0.165$ nm.

As shown in table 1, the particle diameter in the present simulations $D_p = 5\,\mu$m is fixed, and the range of the Hamaker constant is $2.0 \times 10^{-21}\,\text{J} \le A_H \le 5.0 \times 10^{-19}\,\text{J}$, yielding the range of the surface energy $9.8 \times 10^{-4}\,\text{J\,m}^{-2} \le \gamma \le 2.4 \times 10^{-1}\,\text{J\,m}^{-2}$. For typical natural particles, the Tabor parameter values are smaller than 0.03, as listed in table 3. Actually, due to the present values of R_{ij} and $\Delta\gamma$ are very small, the Tabor parameter in the simulations is typically smaller than 0.1, even though the values of the elastic modulus and the Poisson number varied in the wide ranges, i.e. $E > 0.01$ GPa and $0 < \nu_T < 1$. The Johnson–Greenwood mapping introduced by Johnson & Greenwood (1997) indicates that the magnitude of the pull-off force varied continuously from the DMT value for $\mu_T < 0.1$ to the JKR value for $\mu_T > 5$. Hence, the additive DMT model is more appropriate to describe the cohesion and collision between particles for these cases with small Tabor numbers.

Appendix B. Two-way coupled simulations

In order to validate the one-way coupled simulations, we conduct grain-resolved two-way coupled simulations for two typical cases. The immersed boundary method is employed

Type of sediment	E	ν_T	μ_T
Fine sand	5.91 GPa	0.47	3.57×10^{-3}–2.24×10^{-2}
Continental terrace silty clay	3.14 GPa	0.478	4.38×10^{-3}–2.74×10^{-2}
Deep-sea silty clay	3.08 GPa	0.487	4.38×10^{-3}–2.74×10^{-2}

Table 3. Tabor parameter μ_T of typical natural sediments, for the present particle diameter $D_p = 5\,\mu$m, and surface energies ranging from $\gamma = 0.00098$–$0.24\,\mathrm{J\,m^{-2}}$. Values of the elastic modulus E and the Poisson number ν_T are cited from Hamilton (1971).

to describe the particle–fluid interactions as implemented in Vowinckel *et al.* (2019). Sometimes this two-way coupled approach is referred to as 'particle-resolved four-way coupled'. We consider the grain-resolved two-way coupled motion of suspended cohesive particles in three-dimensional, incompressible homogeneous isotropic turbulence. The motion of the single-phase fluid with constant density ρ_f and kinematic viscosity ν is governed by

$$\nabla \cdot \boldsymbol{u_f} = 0, \tag{B1}$$

$$\frac{\partial \boldsymbol{u_f}}{\partial t} + (\boldsymbol{u_f} \cdot \nabla)\boldsymbol{u_f} = -\frac{1}{\rho_f}\nabla p + \nu\nabla^2\boldsymbol{u_f} + \boldsymbol{F}_{tur} + \boldsymbol{F}_{ibm}, \tag{B2}$$

where $\boldsymbol{u_f} = (u_f, v_f, w_f)^{\mathrm{T}}$ denotes the fluid velocity vector and p indicates the hydrodynamic pressure. We employ the spectral approach of Eswaran & Pope (1988) to obtain the forcing term $\boldsymbol{F}_{tur}$, which generates and maintains statistically stationary turbulence, as implemented in Chouippe & Uhlmann (2015). Here, $\boldsymbol{F}_{tur}$ is non-zero only in the low-wavenumber band where the wavenumber vector $|\boldsymbol{\kappa}| < \kappa_f$, with $\kappa_f = 2.3\kappa_0$ and $\kappa_0 = 2\pi/L_0$, with L_0 denoting the length of the physical domain. The origin $\boldsymbol{\kappa} = 0$ is not forced. In addition to the cutoff wavenumber κ_f, the random forcing process is governed by the dimensionless parameter $D_s = \psi^2 T_0 L_0^4/\nu^3$, where ψ^2 and T_0 indicate the variance and the time scale of the random process, respectively. Regarding the details of evaluating $\boldsymbol{F}_{tur}$ from κ_f and D_s, we refer the reader to the original work by Eswaran & Pope (1988); $\boldsymbol{F}_{ibm}$ represents an artificial volume force introduced by the immersed boundary method (Vowinckel *et al.* 2019).

We calculate the motion of each individual spherical particle by solving an ordinary differential equation for its translational velocity and angular velocity,

$$m_p\frac{\mathrm{d}\boldsymbol{u}_{p,i}}{\mathrm{d}t} = \oint_{\Gamma_p} \boldsymbol{\tau}\cdot\boldsymbol{n}\,\mathrm{d}A + \sum_{j=1,j\neq i}^{N}(\boldsymbol{F}_{con,ij} + \boldsymbol{F}_{lub,ij} + \boldsymbol{F}_{coh,ij}), \tag{B3}$$

$$I_p\frac{\mathrm{d}\boldsymbol{\omega}_{p,i}}{\mathrm{d}t} = \oint_{\Gamma_p} \boldsymbol{r}\times(\boldsymbol{\tau}\cdot\boldsymbol{n})\,\mathrm{d}A + \sum_{j=1,j\neq i}^{N}(\boldsymbol{T}_{con,ij} + \boldsymbol{T}_{lub,ij}), \tag{B4}$$

where $\boldsymbol{\tau}$ denotes the hydrodynamic stress tensor, $\boldsymbol{r}$ is the position vector of the surface point with respect to the centre of mass of a particle.

In two-way coupling simulations, we set the number of primary particles $N = 82$ and the size ratio between the domain and the primary particles $L_0/D_p = 102.4$, yielding the volume fraction of particles $\phi \approx 4.0 \times 10^{-5}$. The density ratio $\rho_p/\rho_f = 2.65$ and the cohesive number $Co = 0.5$ are fixed. The triply periodic computational domain is

a cube with the number of grid cells $N_x \times N_y \times N_z = 1024 \times 1024 \times 1024$. The length ratios between the Kolmogorov scale and the size of primary particles are $\eta/D_p = 36$ and $\eta/D_p = 3.3$ for cases L5 and L15, respectively.

REFERENCES

BERGOUGNOUX, L., BOUCHET, G., LOPEZ, D. & GUAZZELLI, E. 2014 The motion of solid spherical particles falling in a cellular flow field at low Stokes number. *Phys. Fluids* **26** (9), 093302.

BIEGERT, E., VOWINCKEL, B. & MEIBURG, E. 2017 A collision model for grain-resolving simulations of flows over dense, mobile, polydisperse granular sediment beds. *J. Comput. Phys.* **340**, 105–127.

BRAITHWAITE, K.M., BOWERS, D.G., NIMMO SMITH, W. & GRAHAM, G.W. 2012 Controls on floc growth in an energetic tidal channel. *J. Geophys. Res.* **117**, C2.

BUBAKOVA, P., PIVOKONSKY, M. & FILIP, P. 2013 Effect of shear rate on aggregate size and structure in the process of aggregation and at steady state. *Powder Technol.* **235**, 540–549.

CHEN, S., LI, S. & MARSHALL, J.S. 2019 Exponential scaling in early-stage agglomeration of adhesive particles in turbulence. *Phys. Rev. Fluids* **4** (2), 024304.

CHOUIPPE, A. & UHLMANN, M. 2015 Forcing homogeneous turbulence in direct numerical simulation of particulate flow with interface resolution and gravity. *Phys. Fluids* **27** (12), 123301.

CHRISTOPHER, P., TRUSHANT, M. & GARETH, M. 2008 High shear rate viscometry. *Rheol. Acta* **47**, 621–642.

DERJAGUIN, B., MULLER, V. & TOPOROV, Y. 1975 Effect of contact deformations on the adhesion of particles. *J. Colloid Interface Sci.* **53** (2), 314–326.

DIZAJI, F.F. & MARSHALL, J.S. 2017 On the significance of two-way coupling in simulation of turbulent particle agglomeration. *Powder Technol.* **318**, 83–94.

DYER, K.R. 1989 Sediment processes in estuaries: future research requirements. *J. Geophys. Res.* **94** (C10), 14327–14339.

ESWARAN, V. & POPE, S.B. 1988 An examination of forcing in direct numerical simulations of turbulence. *Comput. Fluids* **16** (3), 257–278.

HAMILTON, E.L. 1971 Elastic properties of marine sediments. *J. Geophys. Res.* **76** (2), 579–604.

HE, W., NAN, J., LI, H. & LI, S. 2012 Characteristic analysis on temporal evolution of floc size and structure in low-shear flow. *Water Res.* **46**, 509–520.

JOHNSON, K.L. & GREENWOOD, J.A. 1997 An adhesion map for the contact of elastic spheres. *J. Colloid Interface Sci.* **192** (2), 326–333.

JOHNSON, K.L., KENDALL, K. & ROBERTS, A.D. 1971 Surface energy and the contact of elastic solids. *Proc. R. Soc. Lond.* A **324** (1558), 301–313.

KHELIFA, A. & HILL, P. 2006 Kinematic assessment of floc formation using a Monte Carlo model. *J. Hydraul. Res.* **44**, 548–559.

MARKUSSEN, N. & ANDERSEN, J. 2014 Flocculation and floc break-up related to tidally induced turbulent shear in a low-turbidity, microtidal estuary. *J. Sea Res.* **89**, 1–11.

MARSHALL, J.S. & LI, S. 2014 *Adhesive Particle Flow*. Cambridge University Press.

MAXEY, M.R. 1987 The motion of small spherical particles in a cellular flow field. *Phys. Fluids* **30**, 1915–1928.

MIETTA, F., CHASSAGNE, C., MANNING, A. & WINTERWERP, J. 2009 Influence of shear rate, organic matter content, ph and salinity on mud flocculation. *Ocean Dyn.* **59**, 751–763.

SERRA, T., COLOMER, J. & LOGAN, B. 2008 Efficiency of different shear devices on flocculation. *Water Res.* **42**, 1113–1121.

SON, M. & HSU, T.J. 2008 Flocculation model of cohesive sediment using variable fractal dimension. *Environ. Fluid Mech.* **8** (1), 55–71.

SOOS, M., MOUSSA, A., EHRL, L., SEFCIK, J., WU, H. & MORBIDELLI, M. 2008 Effect of shear rate on aggregate size and morphology investigated under turbulent conditions in stirred tank. *J. Colloid Interface Sci.* **319**, 577–589.

SPICER, P., PRATSINIS, S., RAPER, J., AMAL, R., BUSHELL, G. & MEESTERS, G. 1998 Effect of shear schedule on particle size, density, and structure during flocculation in stirred tanks. *Powder Technol.* **97**, 26–34.

STRICOT, M., FILALI, A., LESAGE, N., SPÉRANDIO, M. & CABASSUD, C. 2010 Side-stream membrane bioreactors: influence of stress generated by hydrodynamics on floc structure, supernatant quality and fouling propensity. *Water Res.* **44** (7), 2113–2124.

STROM, K. & KEYVANI, A. 2016 Flocculation in a decaying shear field and its implications for mud removal in near-field river mouth discharges. *J. Geophys. Res.* **121** (4), 2142–2162.

Tabor, D. 1977 Surface forces and surface interactions. In *Colloid and Interface Science, Volume I: Plenary and Invited Lectures*, pp. 3–14. Academic Press.

Tran, D., Kuprenas, R. & Strom, K. 2018 How do changes in suspended sediment concentration alone influence the size of mud flocs under steady turbulent shearing? *Cont. Shelf Res.* **158**, 1–14.

Vowinckel, B., Withers, J., Luzzatto-Fegiz, P. & Meiburg, E. 2019 Settling of cohesive sediment: particle-resolved simulations. *J. Fluid Mech.* **858**, 5–44.

Wang, Z., Nan, J., Ji, X. & Yang, Y. 2018 Effect of the micro-flocculation stage on the flocculation/sedimentation process: the role of shear rate. *Sci. Total Environ.* **633**, 1183–1191.

Winterwerp, J.C. 1998 A simple model for turbulence induced flocculation of cohesive sediment. *J. Hydraul. Res.* **36** (3), 309–326.

Winterwerp, J.C., Manning, A.J., Martens, C., de Mulder, T. & Vanlede, J. 2006 A heuristic formula for turbulence-induced flocculation of cohesive sediment. *Estuar. Coast. Shelf Sci.* **68**, 195–207.

Yao, Y. & Capecelatro, J. 2021 Deagglomeration of cohesive particles by turbulence. *J. Fluid Mech.* **911**, A10.

Zhang, H., Yang, L., Zang, X., Cheng, S. & Zhang, X. 2019 Effect of shear rate on floc characteristics and concentration factors for the harvesting of *Chlorella vulgaris* using coagulation-flocculation-sedimentation. *Sci. Total Environ.* **688**, 811–817.

Zhao, K., Pomes, F., Vowinckel, B., Hsu, T.-J., Bai, B. & Meiburg, E. 2021 Flocculation of suspended cohesive particles in homogeneous isotropic turbulence. *J. Fluid Mech.* **921**, A17.

Zhao, K., Vowinckel, B., Hsu, T.-J., Köllner, T., Bai, B. & Meiburg, E. 2020 An efficient cellular flow model for cohesive particle flocculation in turbulence. *J. Fluid Mech.* **889**, R3.

Zhu, R., He, Z., Zhao, K., Vowinckel, B. & Meiburg, E. 2022 Grain-resolving simulations of submerged cohesive granular collapse. *J. Fluid Mech.* **942**, A49.